Optics Letters

Scanning interferometric near-infrared spectroscopy

Oybek Kholiqov,[1] Wenjun Zhou,[1] Tingwei Zhang,[1] Mingjun Zhao,[1,2] Soroush Ghandiparsi,[1] and Vivek J. Srinivasan[1,2,*]

[1]Department of Biomedical Engineering, University of California Davis, Davis, California 95616, USA
[2]Tech4Health Institute, NYU Langone Health, New York, New York 10010, USA
*Corresponding author: vjsriniv@ucdavis.edu

Received 21 September 2021; revised 4 November 2021; accepted 19 November 2021; posted 19 November 2021; published 21 December 2021

In diffuse optics, quantitative assessment of the human brain is confounded by the skull and scalp. To better understand these superficial tissues, we advance interferometric near-infrared spectroscopy (iNIRS) to form images of the human superficial forehead blood flow index (BFI). We present a null source–collector (S-C) polarization splitting approach that enables galvanometer scanning and eliminates unwanted backscattered light. Images show an order-of-magnitude heterogeneity in superficial dynamics, implying an order-of-magnitude heterogeneity in brain specificity, depending on forehead location. Along the time-of-flight dimension, autocorrelation decay rates support a three-layer model with increasing BFI from the skull to the scalp to the brain. By accurately characterizing superficial tissues, this approach can help improve specificity for the human brain.

https://doi.org/10.1364/OL.443533

Near-infrared (NIR) light provides a convenient and simple means of non-invasive and continuous brain monitoring [1]. In diffuse correlation spectroscopy (DCS) [2], light intensity fluctuations arising from accumulated dynamic phase shifts imparted by moving red blood cells (RBCs) provide a blood flow index (BFI). The BFI is given as αD_B, where α is the fraction of overall momentum transfer that arises from dynamic scattering and D_B is an effective RBC Brownian diffusion coefficient [2].

DCS and related approaches [3] suffer from unknown contributions of superficial extracerebral tissues. Most DCS systems are continuous wave (CW) and measure time-of-flight (TOF)-integrated intensity autocorrelations [2,4,5]. To deal with superficial blood flow, CW-DCS requires approaches such as short source–collector (S-C) pairs that preferentially sample superficial tissue, along with multi-layer models and calibration via probe pressure [6–8]. Recent DCS approaches with TOF discrimination can improve brain specificity [9], but cannot eliminate extracerebral contributions. To describe extracerebral contamination, extracerebral tissues are modeled as one or two layers that nominally represent the scalp and skull [10,11]. A third extracerebral layer for the cerebrospinal fluid is occasionally included [8], though there is no consensus on the best model. To the best of the author's knowledge, no optical technique has yet provided a detailed account of the extracerebral dynamics across the surface of the forehead and in depth.

Interferometric near-infrared spectroscopy (iNIRS) [12,13] measures the TOF-resolved optical field autocorrelation after multiple scattering in tissue. When applied to the forehead, iNIRS recently suggested incipient brain sensitivity at TOFs of 500–600 ps [14]. Here, we further develop iNIRS for multi-dimensional TOF-resolved imaging of the human forehead. To achieve this, a null S-C separation iNIRS system employs polarization splitting [15] for perfect S-C overlap to suppress undesirable single-scattered and few-scattered light.

In iNIRS, the wavelength of a narrow-linewidth laser is rapidly tuned to measure multiply scattered diffuse light paths over tens of centimeters. By measuring the interference spectrum between light traversing the sample tissue and light traversing a reference path, iNIRS reconstructs a mutual coherence function $\Gamma_{rs}(\tau_s, t_d)$, where τ_s is the TOF and t_d is the delay time. The TOF-resolved iNIRS optical field autocorrelation, $G_1^{iNIRS}(\tau_s, \tau_d)$, is obtained from a series of measurements over the delay time (t_d),

$$G_1^{iNIRS}(\tau_s, \tau_d) = \left\langle \Gamma_{rs}^*(\tau_s, t_d)\Gamma_{rs}(\tau_s, t_d + \tau_d)\right\rangle_{t_d}, \quad (1)$$

where τ_d is the time lag and brackets denote the expectation over t_d [16], which is in practice approximated by averaging over a time window. The temporal point-spread function (TPSF) is $G_1^{iNIRS}(\tau_s, 0)$. The TOF-resolved autocorrelation decay rate, $\xi(\tau_s) = -\partial g_1^{iNIRS}(\tau_s, \tau_d = 0^+)/\partial\tau_d$, where

$$g_1^{iNIRS}(\tau_s, \tau_d) = G_1^{iNIRS}(\tau_s, \tau_d)/G_1^{iNIRS}(\tau_s, 0), \quad (2)$$

provides information about the medium dynamics. Note that the zero-lag derivative is highly sensitive to longer paths and well described by the first cumulant approximation of diffusing wave spectroscopy (DWS) [17]. We experimentally determined $\xi(\tau_s)$ from a five-parameter fit [14] of $g_1^{iNIRS}(\tau_s, \tau_d)$ at each TOF. In other words, given $G_1^{iNIRS}(\tau_s, \tau_d) \approx A(\tau_s)e^{-B(\tau s)\tau d} + C(\tau_s)e^{-D(\tau s)\tau d} + E(\tau_s)$, we find that $\xi(\tau_s) \approx [A(\tau_s)B(\tau_s) + C(\tau_s)D(\tau_s)]/[A(\tau_s) + C(\tau_s) + E(\tau_s)]$.

The multi-dimensional data provided by iNIRS at a single S-C separation would be further enhanced by lateral resolution to assess spatial heterogeneity. Here, we introduce an imaging approach for iNIRS. For laterally resolved two-dimensional scanning, we employ a null S-C separation approach.

However, at short S-C separation, the strong superficially backscattered light may obscure deeper paths due to sidelobes in the instrument response function [13]. To enhance the effective dynamic range, we employ a polarization splitting strategy

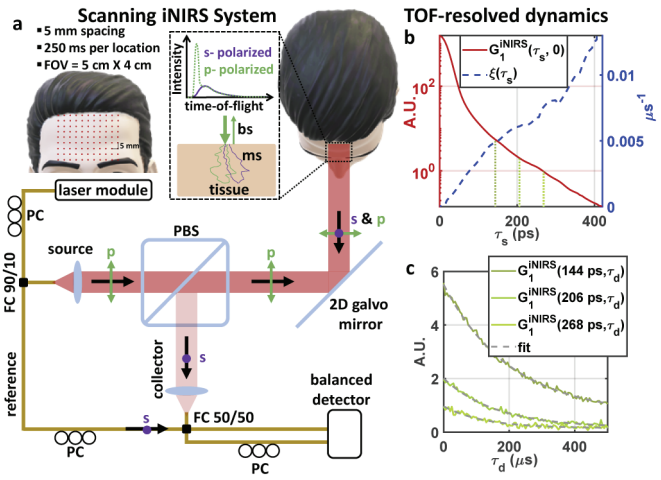

Fig. 1. (a) Scanning iNIRS. A polarization beam splitter (PBS) allows for efficient suppression of single-scattered or few-scattered light (green) and more effective use of the dynamic range of the system to detect multiply scattered light. (b) Example temporal point spread function (TPSF) and corresponding time-of-flight-resolved decay rates determined from field autocorrelations (c) acquired at 200,000 sweeps per second with a 0.25 s averaging window. Visualization 1 shows movies of the data in (b),(c). Dashed gray lines represent 5-parameter [14] bi-exponential fits (PC: polarization controller, FC: fiber coupler, s: sagittal, p: parallel, bs: backscattered light, ms: multiply scattered light).

[Fig. 1(a)]. This approach relies on the fact that backreflected, backscattered, and quasi-backscattered light from the sample generally maintains the incident polarization state [green in Fig. 1(a)]. On the other hand, after a sufficient number of scattering events, multiply scattered light is essentially randomly polarized when observed on a time scale longer than the decorrelation time. We employ a polarizing beam splitter (PBS) from Newport Corporation (10FC16PB.5) with a 500:1 extinction ratio, oriented to reflect the s polarization state to the collector. With a transmitted input p polarization state incident on the sample, the single-scattered and few-scattered light can be preferentially suppressed. The spatial S-C overlap enables the use of a single galvanometer to both scan the source light and de-scan the light returning to a collector across many spatial (x, y) locations in the field of view, forming four-dimensional (x, y, τ_s, τ_d) data sets. First, with a polarization controller, the polarization exiting the source collimator is adjusted to maximize the power on the sample, ensuring incident p polarization [green in Fig. 1(a)] at the PBS. As argued previously, the light from the sample returning in the de-scanned collector mode is distributed into p [green in Fig. 1(a)] and s [purple in Fig. 1(a)] polarization states, with the former containing both backscattered and multiply scattered light and the latter containing just multiply scattered light [inset in the dashed box in Fig. 1(a)]. The p polarization is transmitted back to the source, whereupon it is attenuated by the isolator (not shown) in the laser module. The s polarization is reflected by the PBS to the collection collimator. Finally, by matching the reference polarization state to the polarization state of the collected sample light, mutual coherence and effective sensitivity are optimized at the detector for multiply scattered light (long TOFs). This scheme rejects backscattered light, unlike optical coherence tomography [18].

Data were acquired across the human forehead with an 855 nm commercial distributed-feedback laser [12,13] swept at 100 kHz (5 µs unidirectional sweep or 200,000 sweeps per second) with a 35 ps full-width-at-half-maximum (FWHM) TOF resolution. The scanning protocol deflected the 2-mm FWHM diameter, 20 mW beam laterally across the forehead with the galvanometer pair, parking every 5 mm to perform a 250 ms acquisition. The subject was located 12 cm from the galvanometers. All procedures were approved by the UC Davis Institutional Review Board, skin power density was below the American National Standards Institute maximum permissible exposure, and the subject wore laser safety goggles. A motion detection algorithm parsed and assigned data to individual positions, excluding the Doppler frequency shift [14] artifact induced by stepping the galvanometer. The entire 2D raster scan shown in Fig. 1(a) took 25 s. Each position yielded a rich two-dimensional data set describing the autocorrelation dynamics versus TOF [Figs. 1(b), 1(c)]. Visualization 1 in the supplementary material shows a movie of both the decay rate and the TPSF versus TOF.

To guide the interpretation of experiments, we employed a simple and intuitive expression for the autocorrelation derivative at zero lag, generalized from Eq. S15 of [19]:

$$\xi(\tau_s) = \frac{-\partial g_1(\tau_s, \tau_d = 0^+)}{\partial \tau_d} = 2k^2 \left[\sum_{i=1}^{N} \mathrm{BFI}_i Y_i(\tau_s) \right], \quad (3)$$

where k is the medium wavenumber. According to Eq. (3), the contribution of layer i to the overall autocorrelation decay is proportional to the product of the blood flow index, BFI_i, and the dimensionless momentum transfer, Y_i, in that layer. The latter can be further approximated by $Y_i(\tau_s) \approx \mu'_{s,i} l_i(\tau_s)$ under the condition of diffuse scattering in layer i, where $\mu'_{s,i}$ is the reduced scattering coefficient and $l_i(\tau_s)$ is the path length in layer i. Note that for a single layer ($N = 1$), given $l_1(\tau_s) = v\tau_s$, where v is the speed of light, Eq. (3) reduces to the standard DWS expression [17] modified to accommodate $\mathrm{BFI}_1 = \alpha_1 D_{B,1}$ [2]:

$$\xi(\tau_s) = 2k^2 \mathrm{BFI}_1 \mu'_s v \tau_s, \quad (4)$$

where k is the medium wavenumber. The TOF axis was shifted so the centroid of the measured iNIRS temporal point-spread function $G_1^{\mathrm{iNIRS}}(\tau_s,0)$ equaled the centroid of the theoretical time-resolved diffuse reflectance (~13 ps) for a semi-infinite medium with realistic optical properties ($\mu_a = 0.1\ \mathrm{cm}^{-1}$ and $\mu'_s = 12\ \mathrm{cm}^{-1}$, $g = 0.9$). Fixing the zero-TOF ($\tau_s = 0$) position in this manner enabled us to use a proportional fit (slope only) rather than a linear fit (slope and intercept). If Eq. (4) is valid for early TOFs (< 150 ps), a laterally resolved proportional fit of the decay rate versus TOF yields images of superficial BFI. These images show a notable (order-of-magnitude) superficial BFI variation across the forehead [Fig. 2(a)]. To determine how this heterogeneous superficial BFI might affect brain specificity, a Monte Carlo eXtreme [20] simulation was performed for a two-layer planar geometry (layer 1 was a 1 cm "scalp-skull," referred to as "superficial" or "scalp" for short, and layer 2 was a semi-infinite brain) with $\mu_{a,1} = 0.1\ \mathrm{cm}^{-1}$, $\mu_{a,2} = 0.2\ \mathrm{cm}^{-1}$, $n = 1.4$, $\mu'_s = 12\ \mathrm{cm}^{-1}$, and $g = 0.9$, which yielded TOF-resolved momentum transfers $Y_1(\tau_s)$ and $Y_2(\tau_s)$, with TOF windowing used to approximate the system TOF resolution [21]. The layer i sensitivity was defined as the zero-lag autocorrelation derivative [$\xi(\tau_s)$] change divided by the fractional BFI_i change [22]:

$$\mathrm{sens}_i(\tau_s) = \partial \xi(\tau_s) / \partial \mathrm{BFI}_i \times \mathrm{BFI}_i = 2k^2 \mathrm{BFI}_i Y_i(\tau_s). \quad (5)$$

The sensitivity to layer i in Eq. (5) is equal to the contribution of layer i to the autocorrelation decay rate in Eq. (3). By taking

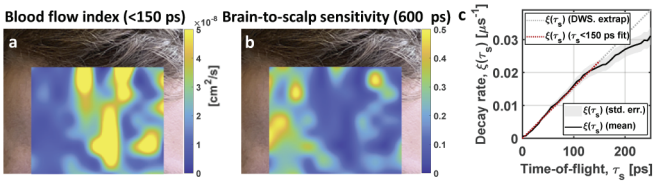

Fig. 2. (a) The superficial blood flow index across the human forehead, determined from the initial slope (0–150 ps) of the autocorrelation decay rate versus TOF using a short (0.25 s) averaging window, exhibits more than an order of magnitude of variation. (b) The brain-to-scalp sensitivity map at 600 ps, obtained from the two-layer model of Eq. (6) with BFI_1 from (a) and $BFI_2 = 1 \times 10^{-7}$ cm^2/s, exhibits comparable heterogeneity, ranging from good (50%) to poor (< 5%). (c) The autocorrelation decay rate versus TOF, averaged across all image points, deviates from an extrapolation of the line of proportionality fitted over the first 150 ps.

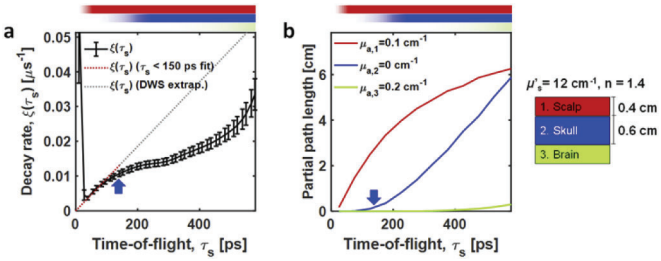

Fig. 3. iNIRS provides direct evidence to support a three-layer model of human head blood flow dynamics. (a) Decay rate versus time-of-flight (TOF) for TOFs up to 600 ps, obtained with a 20 s averaging window. The decay rate versus TOF deviates from an extrapolation of the line of proportionality fitted over the first 150 ps. Therefore, the data violate DWS for a single uniform medium. (b) To interpret layer contributions, partial path lengths for scalp (red/mid-gray), skull (blue/dark gray), and semi-infinite brain (green/light gray) determined from a three-layer Monte Carlo model are plotted against TOF. Partial path lengths are also shown as shaded bars along the top of (a) and (b) to facilitate comparison. Interestingly, the deviation from the proportional trend is first observed around the TOF indicated by the arrow, where the partial path length of the skull first becomes significant. These data support a three-layer model where the skull has a lower blood flow index than the scalp.

BFIs of the superficial layer ($BFI_1 = \alpha_1 D_{B,1}$) from Fig. 2(a), and assuming that brain $BFI_2 = \alpha_2 D_{B,2} = 1 \times 10^{-7}$ cm^2/s, a simple TOF-resolved brain-to-scalp sensitivity [19], or brain specificity, for a two-layer model is given by (where $i = 2$ and $j = 1$):

$$\text{sens}_i(\tau_s)/\text{sens}_j(\tau_s) = [\text{BFI}_i Y_i(\tau_s)]/[\text{BFI}_j Y_j(\tau_s)]. \quad \textbf{(6)}$$

Irrespective of the assumed brain BFI and model geometry, Eq. (6) demonstrates that a 10-fold variability in scalp BFI (BFI_1) [Fig. 2(a)] implies a 10-fold variability in brain specificity. Recall that that the autocorrelation decay rate was taken as the zero-lag derivative, yielding the upper limit of experimentally achievable brain specificity in Eq. (6). The brain-to-scalp sensitivity map at $\tau_s = 600$ ps [Fig. 2(b)] clearly shows regions with higher superficial BFI [Fig. 2(a)] and low brain specificity. Such regions should be avoided when assessing brain BFI.

The TOF-resolved decay rates, when averaged across image locations, tended to plateau at TOFs less than 250 ps [Fig. 2(c)]. This observation was further confirmed by a second-order fit, which yielded negative curvature at 80% of the locations. This behavior contradicts a two-layer model, which predicts a decay rate proportional to TOF for short TOFs, followed by a steeper slope at the onset of brain sensitivity at longer TOFs [14].

Next, a 20 s acquisition was performed at a single location to measure longer TOFs, which have better brain sensitivity. The longer acquisition roughly reproduced the change in the autocorrelation decay rate with TOF [Fig. 3(a)] reported earlier [14], with the late TOF phase at 500–600 ps coinciding with the onset of brain sensitivity. However, deviations from a simple biphasic decay rate versus TOF predicted by a two-layer model [14] [Fig. 3(a)] were noted. At TOFs below 600 ps, iNIRS portrayed a triphasic decay rate versus TOF: (1) an initial proportional increase in the first phase, followed by (2) a flattening in the second phase and (3) a sharp steepening in the third phase.

We recall that for a uniform medium, DWS [Eq. (4)] predicts that the autocorrelation decay rate is proportional to the TOF. Therefore, deviations from a proportional trend imply medium non-uniformities. We hypothesize that the three phases corresponded to the major forehead tissues: (1) scalp, (2) skull, and (3) brain. To assess the feasibility of this hypothesis, we first determined approximate partial path lengths for scalp, skull, and brain from a Monte Carlo eXtreme three-layer planar model of the human head [Fig. 3(b)]. The parameters of the three-layer model were chosen based on reasonable anatomical assumptions (thicknesses of 0.4 cm for the scalp and 0.6 cm for the skull). We found that the skull partial path length in this model first became significant around 150 ps; this is where we expect the decay rate to be first impacted by the skull. We performed a proportional fit to the first 150 ps [red/black dotted line in Fig. 3(a)] to apply DWS to the scalp alone. Interestingly, the extrapolation of the proportional fit [gray dotted line in Fig. 3(a)] began to exceed experimental observations around 150 ps (indicated by the arrow), consistent with scalp BFI exceeding skull BFI.

Having established the plausible need for a three-layer model, we next compared the abilities of the three- and two-layer models to reproduce experimental decay rates versus the TOF. We again simulated [20] the average dimensionless momentum transfer $Y_i(\tau_s)$ for each layer (indexed by i) in both the three-layer ($N = 3$) and the two-layer ($N = 2$) models with the parameters given in Fig. 4. We varied layer thicknesses and BFI values with the constraint that the skull BFI (BFI_2) for the three-layer ($N = 3$) model was zero [8]. We found that a three-layer model reproduced experimental observations well ($R^2 = 0.965$) with a scalp thickness of 0.2 cm, a skull thickness of 0.7 cm [Fig. 4(a)], and a brain-to-scalp BFI ratio of 5, which is physiologically reasonable [23]. On the other hand, a two-layer model could not produce the three experimental phases. The best agreement with experiment ($R^2 = 0.421$) was achieved with a brain-to-scalp BFI ratio of > 20, which seems unreasonable [Fig. 4(b)], for non-contact measurements without compression. These results support the three-layer model to model adult human head dynamics.

Note that while the superficial layers are referred to as "scalp" and "skull" here for convenience, the scalp itself comprises multiple layers. Thus, we must distinguish between model layers and anatomical layers. It is interesting to note that a model scalp just 2 mm in thickness, thinner than the anatomical scalp, and a skull BFI of zero reproduce the early TOF experimental observations quite well. Thus, model layer 1 may account for just the superficial anatomical scalp, while the 7-mm-thick model layer 2 may account for the deeper anatomical scalp and the anatomical skull, as well as, potentially, cerebrospinal fluid (CSF). Though

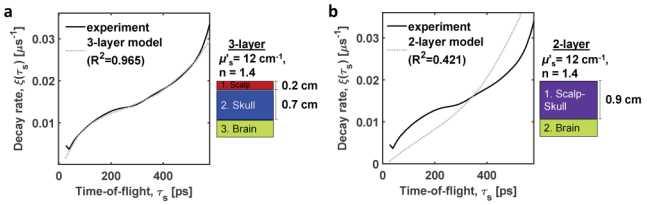

Fig. 4. A three-layer model can reproduce experimental observations, but a two-layer model cannot. (a) A three-layer model [Eq. (3) with $N = 3$] with $BFI_1 = 2.3 \times 10^{-8}$ cm^2/s ($\mu_{a,1} = 0.1$ cm^{-1}), $BFI_2 = 0$ cm^2/s ($\mu_{a,2} = 0$ cm^{-1}), and $BFI_3 = 1.1 \times 10^{-7}$ cm^2/s ($\mu_{a,3} = 0.2$ cm^{-1}) recapitulates the triphasic experimental autocorrelation decay rate versus TOF. (b) On the other hand, a two-layer model [Eq. (3) with $N = 2$] can only produce two phases. A representative two-layer model with $BFI_1 = 7.5 \times 10^{-9}$ cm^2/s ($\mu_{a,1} = 0.1$ cm^{-1}) and $BFI_2 = 1.7 \times 10^{-7}$ cm^2/s ($\mu_{a,2} = 0.2$ cm^{-1}) is shown.

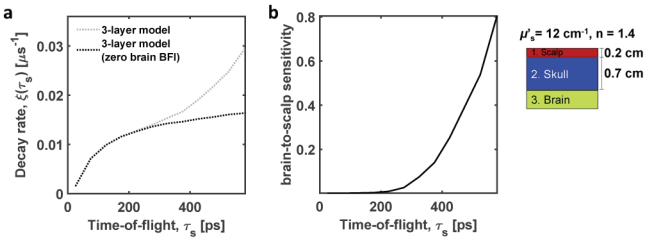

Fig. 5. Predictions of the three-layer model supported by experiments [Fig. 4(a)]. (a) The three-layer model [Eq. (3) with $N = 3$] is reproduced from Fig. 4(a) (gray dotted line). Setting the brain BFI (BFI_3) to zero in Eq. (3) (black dotted line), we discover that brain BFI contributes to the autocorrelation decay rate as early as 450 ps and accounts for 44% of the decay rate around 580 ps, where the brain-to-scalp sensitivity reaches 80% (b). The prediction in (b), based on the zero-lag autocorrelation derivative, represents the best achievable brain specificity, which can only be approached by conventional fitting methods [22].

neglecting layer 2 dynamics altogether is an approximation, the average data [Fig. 2(c)] suggest that skull BFI is lower superficial scalp BFI, in spite of significant heterogeneity [Fig. 2(b)].

We next employed the three-layer model to predict what would happen if the brain BFI_3 were zero [Fig. 5(a)]. Brain specificity [Fig. 5(b)] was also determined from Eq. (6) with $i = 3$ and $j = 1$. Interestingly, the autocorrelation decay rate was found to be sensitive to the brain as early as 450 ps, with a more than 25% brain specificity [Fig. 5(b)]. At first, this seems surprising, since the partial path length and momentum transfer of photons in the brain are small. Yet, we are reminded by the sensitivity expression [Eq. (5)] that a small brain momentum transfer can be offset by a large brain BFI. The large predicted brain specificity is also driven by the low layer 1 momentum transfer in the three-layer model, since the layer 1 thickness is only 2 mm.

In summary, we imaged TOF-resolved and laterally resolved diffuse optical field correlations from the human forehead. Our images identify areas with low superficial dynamics, which represent optimal regions to target for high-specificity brain monitoring with CW techniques. Unlike TOF gating methods [9], iNIRS provides fine TOF resolution, revealing a triphasic pattern of dynamics, in support of a three-layer model with scalp blood flow exceeding skull blood flow. Although iNIRS cannot eliminate extracerebral signals, Fig. 4(a) suggests that the fine TOF resolution of iNIRS may enable the separation of cerebral and extracerebral dynamics by model fitting; however, this model awaits ground-truth validation. Additional simulations (not shown) suggest that adding a 2 mm CSF layer can alter TOF-resolved autocorrelations, though the triphasic shape remains intact. The lack of validation of "model layers" against anatomy is a study limitation. Lastly, though brain specificity could be achieved at single locations, speed is presently photon limited due to single-mode detection, and imaging of brain dynamics was not performed.

Funding. National Institutes of Health (EB029747, EY031469).

Disclosures. The authors declare no conflicts of interest.

Data availability. Data underlying the results presented in this paper may be obtained from the authors upon reasonable request.

REFERENCES

1. F. F. Jobsis, Science **198**, 1264 (1977).
2. D. A. Boas and A. G. Yodh, J. Opt. Soc. Am. A **14**, 192 (1997).
3. J. Xu, A. K. Jahromi, J. Brake, J. E. Robinson, and C. Yang, APL Photonics **5**, 126102 (2020).
4. D. A. Boas, L. Campbell, and A. G. Yodh, Phys. Rev. Lett. **75**, 1855 (1995).
5. L. He, W. B. Baker, D. Milej, V. C. Kavuri, R. C. Mesquita, D. R. Busch, K. Abramson, J. Y. Jiang, M. Diop, K. St. Lawrence, O. Amendolia, F. Quattrone, R. Balu, W. A. Kofke, and A. G. Yodh, Neurophotonics **5**, 045006 (2018).
6. W. B. Baker, A. B. Parthasarathy, T. S. Ko, D. R. Busch, K. Abramson, S. Y. Tzeng, R. C. Mesquita, T. Durduran, J. H. Greenberg, D. K. Kung, and A. G. Yodh, Neurophotonics **2**, 035004 (2015).
7. D. Milej, A. Abdalmalak, A. Rajaram, and K. St Lawrence, Neurophotonics **7**, 045002 (2020).
8. M. M. Wu, S.-T. Chan, D. Mazumder, D. Tamborini, K. Stephens, B. Deng, P. Farzam, Y. Chu, M. A. Franceschini, J. Qu, and S. A. Carp, Neurophotonics **8**, 015001 (2021).
9. M. Pagliazzi, S. K. V. Sekar, L. Colombo, E. Martinenghi, J. Minnema, R. Erdmann, D. Contini, A. Dalla Mora, A. Torricelli, and A. Pifferi, Biomed. Opt. Express **8**, 5311 (2017).
10. W. B. Baker, A. B. Parthasarathy, D. R. Busch, R. C. Mesquita, J. H. Greenberg, and A. G. Yodh, Biomed. Opt. Express **5**, 4053 (2014).
11. K. Verdecchia, M. Diop, A. Lee, L. B. Morrison, T. Y. Lee, and K. St Lawrence, Biomed. Opt. Express **7**, 3659 (2016).
12. D. Borycki, O. Kholiqov, S. P. Chong, and V. J. Srinivasan, Opt. Express **24**, 329 (2016).
13. O. Kholiqov, D. Borycki, and V. J. Srinivasan, Opt. Express **25**, 28567 (2017).
14. O. Kholiqov, W. Zhou, T. Zhang, V. N. Du Le, and V. J. Srinivasan, Nat. Commun. **11**, 391 (2020).
15. S. L. Jacques, J. C. Ramella-Roman, and K. Lee, J. Biomed. Opt. **7**, 329 (2002).
16. D. Borycki, O. Kholiqov, and V. J. Srinivasan, Optica **3**, 1471 (2016).
17. D. J. Pine, D. A. Weitz, P. M. Chaikin, and E. Herbolzheimer, Phys. Rev. Lett. **60**, 1134 (1988).
18. J. G. Fujimoto, C. Pitris, S. A. Boppart, and M. E. Brezinski, Neoplasia **2**, 9 (2000).
19. W. Zhou, O. Kholiqov, J. Zhu, M. Zhao, L. L. Zimmermann, R. M. Martin, B. G. Lyeth, and V. J. Srinivasan, Sci. Adv. **7**, eabe0150 (2021).
20. S. Yan and Q. Fang, Biomed. Opt. Express **11**, 6262 (2020).
21. D. Mazumder, M. M. Wu, N. Ozana, D. Tamborini, M. A. Franceschini, and S. A. Carp, Neurophotonics **8**, 035005 (2021).
22. J. Selb, D. A. Boas, S. T. Chan, K. C. Evans, E. M. Buckley, and S. A. Carp, Neurophotonics **1**, 015005 (2014).
23. E. Ohmae, Y. Ouchi, M. Oda, T. Suzuki, S. Nobesawa, T. Kanno, E. Yoshikawa, M. Futatsubashi, Y. Ueda, H. Okada, and Y. Yamashita, NeuroImage **29**, 697 (2006).